Two-dimensional, hybrid model of low-pressure glow discharges

A. Fiala, L. C. Pitchford, and J. P. Boeuf
Centre de Physique Atomique, 118 route de Narbonne, 31062 Toulouse CEDEX, France
(Received 12 November 1993)

A self-consistent, two-dimensional hybrid fluid-particle model is presented and used to describe the electrical behavior of dc low-pressure discharges in the current range 10^{-7}–10^{-2} A in argon for products of the gas pressure and the gap spacing (pd) from 1 to 3.3 cm torr. The two-dimensional distributions of the potential, charged particle densities and ionization source term at steady state are shown to illustrate the discharge behavior during the transition from the normal to the abnormal regimes. For the larger values of pd, a positive column region as well as the cathode regions are clearly apparent. The model used here consists of Poisson's equation for the electric field coupled to the continuity equations for the electrons and ions with the important feature that the ionization source term appearing in the continuity equations is nonlocal and determined from a Monte Carlo simulation. This description yields a unified physical picture of discharge behavior in the cathode fall, negative glow, and positive column regions over a wide range of discharge currents.

PACS number(s): 52.65.+z, 52.80.Hc

I. INTRODUCTION

The goal in the work presented here has been to study low-pressure discharge behavior using a two-dimensional (2D) numerical model which is capable of yielding a self-consistent unified description of a low-pressure glow discharge including the cathode fall, the negative glow, and the positive column. Although most of the qualitative features of the results discussed below are known from experiments and previous models, this work serves to quantify the two-dimensional aspects of steady-state glow discharges and it is intended to provide points for comparison with simpler 1D or analytical models. This work goes a step beyond previously published models in that the kinetic description of the ionization source term used here is needed to predict the field reversals on the discharge axis which occur in certain cases.

A comprehensive review of previous modeling of gas discharges (dc and rf) has been recently published by Lister [1], and the book by Raizer [2] gives an excellent and detailed discussion of the physics of glow discharges. We therefore limit our discussion in this section to a summary of the context of the results presented here and refer the reader to these recent publications for a complete discussion of the physics of low-pressure discharges [2] and state-of-the-art modeling [1].

Visually, self-sustained, low-pressure glow discharges consist of several luminous regions which differ in intensity and color and which are clearly separated from each other by regions in which essentially no light is emitted. The diverse regions of emitted radiation of different intensity exist as a result of a distribution of the potential between the electrodes. That is, a large drop in the potential (typically some hundreds of volts) occurs immediately adjacent to the cathode surface in a distance on the order of several ionization mean free paths or less. This cathode fall is followed by a region of near zero and, in some cases, electric field of reversed sign where much of the energy gained by the electrons in accelerating through the cathode fall potential is lost in collisions with the background neutral gas. The properties of the cathode fall and negative glow regions are independent of the discharge length provided it is not too short. The region including the cathode fall and the negative glow will be termed the "cathode region" in the following. If the distance between the electrodes is significantly longer than the cathode region and if charged particle losses exist (diffusion to the walls, recombination), a positive column region appears between the negative glow and the anode. The difference in nature between the negative glow and the positive column plasmas is related to the fact that the negative glow is sustained by electrons coming from the sheath while the positive column is sustained by electrons gaining energy in the local field.

The properties of the cathode region of glow discharges are a direct consequence of the requirement that the discharge be self-sustained. Electrons are emitted from the cathode by secondary electron emission due to bombardment by ions (as well as photons and metastable atoms). These electrons gain energy in accelerating through the cathode fall and deposit energy in the gas in the form of excitation and ionization. The ions thus produced drift back to the cathode and cause emission of secondary electrons with an efficiency typically on the order of 0.1 or fewer electrons emitted per incident ion. The distribution of the potential in the gap is exactly what is needed to assure that, on the average, each electron emitted from the cathode will create enough ions in the volume through ionization which return to the cathode to replace itself. It is possible to argue in 1D that only one stable configuration of the field exists for a given voltage (and gas composition and secondary electron emission from the cathode) which will satisfy the replacement condition, but such an argument is more difficult in 2D where charged particle losses to the walls also play a role in the particle balance.

Perhaps the most remarkable property of low-pressure discharges is that there exists a range of currents for which the current density near the axis at the cathode surface is constant and an increasing discharge current is achieved at a constant voltage by increasing the area of the discharge on the surface. Discharges with this property are termed normal discharges. Higher current glow discharges, termed abnormal glow discharges, occur when the discharge has expanded to fill the entire cathode surface. Further increases in the current in the abnormal discharge regime require an increasing voltage, and the current density at the cathode surface increases. Models of normal discharges are necessarily 2D while 1D models of the abnormal glow are often quite reasonable.

Previous 2D models of low pressure, dc glow discharges, have been published by Boeuf [3] and by Raizer and Surzhikov [4]. Both of these models assume that the ionization source term is a function of the local value of the reduced electric field, E/p, where E is the magnitude of the field and p is the gas pressure. (This is commonly referred to as the local field approximation.) Although these models predicted fairly well the global features of 2D discharges as described below, neither model was capable of describing accurately the negative glow region where the ionization source term depends on the potential distribution upstream in the cathode fall and not on the local value of E/p. Results from one-dimensional models have been published [5] in which the high energy electrons, those capable of producing ionization, are treated separately from the cold, bulk electrons in order to more accurately predict the negative glow region of the discharge. These results confirm the importance of the nonlocal ionization in the glow region.

In this paper, we present results from a 2D, hybrid fluid-particle model with the important feature being that the source term for volume ionization is determined through a Monte Carlo simulation of the cathode emitted electrons and their progeny. This treatment of the high energy electrons provides an accurate description of the nonlocal ionization processes in the cathode regions of the discharges. We describe in Sec. II the hybrid-fluid particle model and the numerical solution scheme. In Sec. III we present results of calculations of the 2D potential, charged particle density distributions, and ionization rate in low-pressure (1 and 3 torr) discharges in argon over a range of currents from 10^{-7} to 10^{-2} A to illustrate the transition from normal (low current) to abnormal (high current) glow discharges and for longer discharges where a transition to a positive column is observed. A discussion of the results is given in Sec. IV, and Sec. V contains a brief summary.

II. DESCRIPTION OF THE MODEL AND NUMERICAL ALGORITHM

A. Physical model

The model described here concerns the electrical properties of glow discharges. The variables are the electron and ion densities and the electric field (or rather the potential) which are functions of two spatial dimensions (assuming cylindrical symmetry) and time. Given the solution for the spatial dependence of these three variables, all electrical properties of the discharge can be deduced. Excitation of the neutral atoms and changes in the gas temperature are neglected.

The ions are described by the first two moments of the Boltzmann equation, the continuity and momentum transfer equations, with the ion flux supposed to be equal to a mobility term and a diffusion term and the drift and diffusion coefficients being given as functions of the local value of the reduced field, $\mathbf{E}(\mathbf{r},t)/p$ (the local field approximation). Although this drift-diffusion representation of the ion flux may not accurately describe ion transport at the cathode fall–negative glow boundary, it generally gives a good representation of the ion velocity in the sheath where the drift velocity is dominant and can be approximated, as shown by Lawler [6], by the equilibrium (local field) velocity. This description fails for very large sheath voltages and short sheath lengths where the ions are nearly collisionless in the sheath and inertia effects dominate. The drift-diffusion representation of the ion transport, however, is expected to be valid over the range of discharge conditions described below.

As just described for the ions, the low energy bulk electrons are also represented using a two moment description with the flux equal to mobility and diffusion terms. The "bulk" electrons determine the electron space charge and the discharge conductivity but do not contribute to the ionization. Because of their smaller mass, the neglect of the electron inertia terms is less of a limitation than the neglect of the ion inertia terms. We do not include an energy equation for the bulk electrons. The electron characteristic energy, the ratio of the diffusion coefficient to the mobility, D_-/μ_-, is fixed and equal to 1 eV. Use of the local field approximation for D_-/μ_- would lead to the electrons unrealistically gaining energy as they diffuse against the field in the cathode sheath and arrive in regions of higher field. Since, as described below, the ionization source term is obtained directly from a particle model, the assumption of a constant electron characteristic energy has only limited consequences on the results.

The most important and distinctive feature of this model is the treatment of the high energy electrons. Since the ionization source term is an extremely sensitive function of the high energy tail of the electron distribution function and since the electron and ion densities increase exponentially with this source term, it is essential to accurately represent this part of the distribution. Furthermore, a good representation of the ionization rate in the cathode region is essential not only for quantitative accuracy, but also for a realistic physical description of the discharge. For example, the nonlocal nature of the ionization rate in the cathode region is fundamental and is entirely responsible for the existence of the negative glow. In the cathode regions of the discharge, the high energy part of the electron distribution cannot be simply characterized either by the mean electron energy which reflects primarily the bulk electrons or the local value of the reduced field. This is especially true under conditions where the ionization mean free path is on the order of or larger than the characteristic length of variation in the

electric field as occurs in the cathode regions of low-pressure discharges. For these reasons, the behavior of the high energy electrons and, hence, the ionization source term, is obtained, in our model, from a particle (Monte Carlo) simulation.

The fundamental variables (the electron density n_-, the positive ion density n_+, and the potential V) are solutions of the following equations: the electron and positive ion continuity equations,

$$\frac{\partial n_-}{\partial t}+\nabla\cdot n_-\mathbf{v}_-=S\ , \tag{1}$$

$$\frac{\partial n_+}{\partial t}+\nabla\cdot n_+\mathbf{v}_+=S\ , \tag{2}$$

and Poisson's equation

$$\Delta V=-\frac{e}{\varepsilon_0}(n_+-n_-)\ , \tag{3}$$

where $\mathbf{v}_{-(+)}$ is the electron (ion) mean velocity, S is the ionization source term (number of electron-ion pairs created per cubic centimeter per second), and e and ε_0 represent the electronic charge and the permittivity of free space, respectively. The second moment of the Boltzmann equation, the momentum transfer equation, is used to calculate the charged particle mean velocities and is represented as the sum of a drift term and a diffusion term

$$\begin{aligned}\phi_{-(+)}&=n_{-(+)}\mathbf{v}_{-(+)}\\&=s_{-(+)}n_{-(+)}\mu_{-(+)}\mathbf{E}-\nabla[n_{-(+)}D_{-(+)}]\ ,\end{aligned} \tag{4}$$

where $s_{-(+)}$ is -1 for electrons ($+1$ for positive ions), $\mu_{-(+)}$ is the electron (ion) mobility, and $D_{-(+)}$ is the coefficient of electron (ion) free diffusion.

The Monte Carlo (MC) simulation is used to describe the behavior of high energy electrons from which the ionization source term is deduced. The term "high energy electrons" is meant to imply those electrons which can produce further ionization, i.e., electrons with a kinetic plus potential energy (the energy equivalent of the difference between the anode potential and the local potential) at a given point larger than the ionization threshold. The accuracy provided by a particle treatment of the electrons is computationally costly, and, in order to reduce the computational time, we simulate only the high energy part of the electron energy distribution and not the full electron energy distribution (from which one could also derive the transport properties of the low energy electrons). Input to the Monte Carlo simulation consists of the 2D electric field distribution and the distribution of secondary electron current density emitted from the cathode which are provided by the fluid model. The MC simulation calculates the trajectories of the cathode emitted electrons and their progeny, and the ionization source term is obtained by integration along the trajectories. Electrons are removed from the simulation when they (a) reach a boundary, (b) are no longer capable of producing ionization, or (c) are trapped in a region where there is a field reversal. (A better treatment of the regions of field reversals where the electrons are trapped would require the inclusion of Coulomb collisions.)

B. Numerical solution of the fluid equations

The continuity equations for the charged particles and Poisson's equation for the electric field are solved self-consistently using an implicit integration scheme for computational efficiency. These equations are cast into a finite-difference representation and solved using an algorithm which was developed in the context of the modeling of semiconductor devices [7,8]. The main features of the solution technique are described in the Appendix.

The algorithm described in the Appendix is implicit (simultaneous solution of Poisson's equation and continuity equations) and can be considerably faster than explicit techniques when the charged particle densities are large. Explicit methods (successive solutions of Poisson's equation and continuity equations) do not take into account the variations of the electric field during the motion of the charged particles, and thus, the integration time step must be shorter than the dielectric relaxation time, τ_d, which is inversely proportional to the electron density:

$$\tau_d=\frac{\varepsilon_0}{e(n_-\mu_-+n_+\mu_+)}\approx\frac{\varepsilon_0}{e(n_-\mu_-)}\ . \tag{5}$$

Therefore, it is not practical to follow the evolution of a high density plasma on long time scales using an explicit method. In our case, using this implicit technique, the integration time step is limited by the time for which the linearization of the continuity equations is valid. According to Kurata [7], the strongest nonlinearity in Eq. (A7) of the Appendix is proportional to the displacement current, and hence the integration time step can be quite long near the steady state. Since times on the order of the ambipolar diffusion time (some 10^{-4} to 10^{-3} sec) are required for the discharge to reach the steady state, it is important to have an integration time step as large as possible.

A comparison of the integration time step Δt used in our implicit fluid model (for the calculation corresponding to the point $b6$ in Fig. 1) and the dielectric relaxation

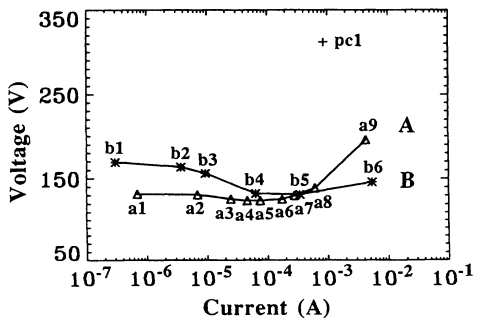

FIG. 1. Voltage-current characteristics for $p=1$ torr ($\triangle$) and $p=3$ torr ($*$). The point indicated by the symbol "+" denotes the calculation with positive column for $p=1.1$ torr and for a discharge tube radius of 1 cm ($pc1$).

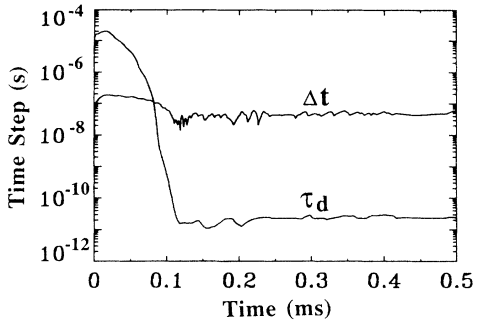

FIG. 2. Time step Δt used in the fluid model as a function of time during the approach to the steady state for the conditions of point *b6* in Fig. 1. For comparison, the dielectric relaxation time, τ_d, the upper limit of the time step in explicit integration schemes, is also shown.

time τ_d, the upper limit on the integration time step in a completely explicit integration algorithm, is shown in Fig. 2. At early times, the electron density is still low and τ_d is therefore rather large. As the discharge evolves, the electron density increases and τ_d correspondingly decreases to values on the order of 10^{-11} sec. The integration time step Δt, however, remains on the order of 10 ns. The gain due to the longer integration times in implicit techniques is offset slightly by the fact that system must be resolved several times per time step; several Newton iterations are required for convergence.

C. Monte Carlo simulation

If the electric field is one dimensional, the electron trajectories (in 3D) can be obtained analytically if one assumes a constant or linearly varying field between two grid points. Due to the two-dimensional geometry here, the electric field is more complex and the electron trajectories must be integrated numerically. In all other respects, the simulation algorithm used here is based on that described by Boeuf and Marode [9]. The coupling to the fluid equations is described by Boeuf and Pitchford [10] and is summarized below.

The integration time step in the fluid equations is small enough that the change in the source term due to the evolution of field distribution between two successive time steps in the fluid model is quite small. Therefore, the ionization source is recalculated by the MC simulation after a certain number of time steps in the integration of the fluid equations, typically several hundred. The ionization source term between two successive calls of the MC is updated after each integration time step in the fluid equations according to

$$S(\mathbf{r},t+\Delta t)=S(\mathbf{r},t)\frac{F(t+\Delta t)}{F(t)}\ , \tag{6}$$

where $F(t)$ is the number of cathode emitted electrons per unit time and Δt is the integration time step in the fluid equations. By doing this, we take into account changes in the cathode emitted electron current between t and $t+\Delta t$, but not the evolution of the potential distribution (which influences the source term on a longer time scale). These considerations are important in reducing the computational time and do not influence at all the steady-state behavior.

An important consideration in all Monte Carlo simulations is statistics. A good compromise between statistical accuracy and computational time must be reached, and it is important to use the information available in the simulation efficiently. To this end, we calculate the ionization source term as a sum of the integrals of the energy dependent ionization frequency over the trajectories of each electron. When properly normalized to the electron current leaving the cathode, this yields the ionization source term in units of per cubic centimeter per second. Alternatively, the ionization source term could be determined from a 2D histogram of the position of the ionization events, but this does not take maximum advantage of the information available in the numerical trajectories and it is consequently less precise for the same computational time. For the calculations reported here, the trajectories of typically 300 cathode emitted electrons and the secondaries created by these electrons were simulated at each call to the Monte Carlo routine. Near the steady state, the simulation was performed less frequently and with a larger number of electrons. The 2D steady-state ionization source terms shown below were calculated using approximately 500 cathode emitted electrons.

D. Boundary conditions and input data

The boundary conditions on the fundamental variables in the fluid equations are zero charged particle densities on the walls and on the electrodes, zero potential on the cathode, the applied potential on the anode, and a floating potential on the dielectric walls. The walls are assumed to be perfect dielectrics (instantaneous recombination of charged particles within the same surface element on the walls and zero conductivity between surface elements). Secondary electron emission at the cathode is assumed to be the result of ion bombardment with a secondary electron emission coefficient (the ratio of the electron current to the ion current at the cathode) of 0.07. The secondary electrons are assumed to be emitte perpendicular to the cathode surface with energy equal to 1 eV. Reflection and secondary emission of electrons from the dielectric walls and the anode are neglected. The gas temperature is supposed to be 273 K.

Input data to the fluid equations are the diffusion coefficient and the mobility as functions of the reduced field E/p. The diffusion coefficients are $D_- = 3\times10^5 p^{-1}$ $\mathrm{cm^2\,s^{-1}}$ for the electrons and $D_+ = 2\times10^2 p^{-1}$ $\mathrm{cm^2\,s^{-1}}$ for the ions where p is the neutral pressure in units of torr. The electron mobility is constant, $\mu_- = 3\times10^5 p^{-1}\,\mathrm{cm^2\,V^{-1}\,s^{-1}}$, and the ion mobility is a function of the reduced electric field as given by Ward [11],

$$\mu_+ = \frac{10^3(1-2.22\times10^{-3}E/p)}{p}\ \mathrm{cm^2\,V^{-1}\,s^{-1}}$$

$$\text{for } E/p \le 60\ \mathrm{V\,cm^{-1}\,torr^{-1}} \text{ and } p \text{ in torr},$$

$$\mu_+ = \frac{8.25\times10^3}{p\sqrt{E/p}}\left[1-\frac{86.52}{(E/p)^{3/2}}\right]\ \mathrm{cm^2\,V^{-1}\,s^{-1}} \tag{7}$$

$$\text{for } E/p > 60\ \mathrm{V\,cm^{-1}\,torr^{-1}} \text{ and } p \text{ in torr}\ .$$

The electron-ion recombination coefficient is small for atomic ions (the density of molecular ions is negligible at the pressures considered here) in a rare gas and was equal to zero in the results reported below. (In an interim report of these results [12], the recombination coefficient was set equal to $2\times10^{-7}\ \mathrm{cm^{-3}\,sec^{-1}}$. The effects of this rather high rate of recombination were small changes in the electric field in the cathode region and a small decrease in the charged particle densities compared to the calculations reported below. More significantly, the sheath length and axial current density on the cathode in the normal regime were constant within numerical precision for the calculation with recombination but increasing slightly with increasing current without recombination, and the axial field in the positive column increased by $3\ \mathrm{V\,cm^{-1}}$ when recombination was included.)

Input data required for the Monte Carlo simulation are the electron neutral scattering cross sections, and we used the cross sections for argon [13] shown in Fig. 3. Electron scattering in inelastic collisions was assumed to be isotropic, and based on previous results in helium [14], we expect this to be reasonably accurate over the range of discharged voltages considered. Effects of anisotropy in elastic scattering are taken into account in the Monte Carlo simulation by using the elastic momentum transfer cross section (rather than the total cross section for elastic scattering) and supposing isotropic scattering. This is justified by recalling that, in a two-term Legendre expansion of the Boltzmann equation, the electron energy distribution function is independent of the total elastic scattering cross section for a given elastic momentum transfer cross section [15].

It is also necessary to specify in the Monte Carlo simulation the distribution of the available energy between the two electrons exiting an ionization event. The energies of the primary and secondary electrons resulting from an ionization event were determined in our simulations from the form given in Refs. [16] and [17]. This form is particularly convenient in Monte Carlo calculations because it yields an analytical expression for the primary ($\varepsilon_{\text{primary}}$) and secondary ($\varepsilon_{\text{secondary}}$) electron energies in terms of a random number, r, between 0 and 1,

$$\varepsilon_{\text{secondary}} = \omega \tan\left\{ r \arctan\left[\frac{\varepsilon_{\text{incident}} - \varepsilon_{\text{IP}}}{2\omega} \right] \right\},$$

$$\varepsilon_{\text{primary}} = \varepsilon_{\text{incident}} - \varepsilon_{\text{IP}} - \varepsilon_{\text{secondary}}\ , \tag{8}$$

where $\varepsilon_{\text{incident}}$ is the incident electron energy and ε_{IP} is the ionization potential. The experimental data in argon [17] are well represented by the above expression with $\omega = 15$ [18]. (Best fits to the experimental data [17] in helium, nitrogen, hydrogen, and oxygen are obtained with values of ω of 15, 13, 14, and 17, respectively [16,18].)

The calculations were all run on an HP series 700 workstation. The total execution time was typically some 500 min (for a 25 by 25 nonuniform grid). Reductions of factors of 2 to 5 in the execution time have recently been achieved in a few test cases by using a different time scale for the electrons and the ions.

III. RESULTS

Two-dimensional distributions of the potential, charged particle densities, and the ionization source term calculated using the hybrid fluid-particle model described above are reported here for glow discharges in argon for pd from 1 to 3.3 torr cm and in the current range from 10^{-7} to 10^{-2} amps. The electrode geometry in all cases is plane and parallel, and cylindrical symmetry is imposed. We first show the discharge behavior as a function of current to illustrate the changes in the internal properties of the discharge during the transition from the normal to the abnormal discharge regime. We then present results in longer discharges to show the transition to a positive column. Note that the sign of the electric field is reversed in the figures and in their description in the text; thus, a "negative" field in the figures and in the text is such as to pull electrons in the direction of the cathode.

A. Discharge behavior as a function of current

In this section, we report a series of calculations for discharges of different current in 1 or 3 torr argon as indicated. The electrodes are 3 cm in diameter and are separated by a distance of 1 cm.

The voltage-current (V-I) characteristics of the 1 and 3 torr discharges, determined by varying a series resistor, are shown in Fig. 1. These calculated characteristics display the well-known features [2,19,20] alluded to in the Introduction; a negative slope in the transition from a Townsend to normal discharge, an almost flat characteristic in the normal glow regime, and a positive characteristic for the higher current abnormal glow regime. The structure in the V-I characteristic is more pro-

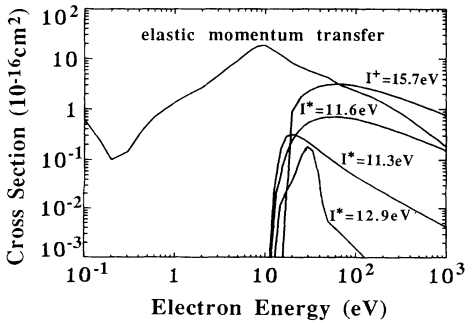

FIG. 3. Cross sections for electron scattering in argon as a function of electron energy as used in these calculations.

TABLE I. Calculated properties of steady-state discharges along the current-voltage characteristic A in Fig. 1 ($p=1$ torr). I is the discharge current, V_a is the anode potential, E_c is the axial field on the cathode, d_c is the sheath length on the axis, x_r is the axial position of the first field reversal, M is the multiplication, and $n_e(p)$ is the maximal electron (positive ion) density.

	$p=1$ torr							
	I (μA)	V_a (V)	E_c (V/cm)	d_c (cm)	x_r (cm)	M	n_e (cm^{-3})	n_p (cm^{-3})
$a3$	24.7	125.8	388	0.59	0.86	16.1	1.4×10^8	4.7×10^8
$a4$	46.1	124.0	511	0.44	0.63	16.2	5.2×10^8	7.4×10^8
$a5$	76.0	123.9	587	0.40	0.60	16.1	6.6×10^8	9.5×10^8
$a8$	610.3	138.9	1137	0.22	0.34	16.4	8.2×10^9	

nounced at 3 torr than at 1 torr, as observed experimentally [21]. Excellent quantitative agreement has been found between calculations using this model and recent measurements of the voltage-current characteristic in abnormal discharges in argon [22].

In the remainder of this section, points on these characteristics will be examined in detail. Selected numerical results along the characteristics are given in Table I (1 torr) and Table II (3 torr).

1. *Results for 1 torr*

In this section, the points along the characteristic A in Fig. 1 corresponding to argon at 1 torr and an electrode separation of 1 cm are discussed.

The lowest current point $a1$ corresponds to the classical Townsend regime where the space charge distortion of the geometrical electric field is negligible. The maxima of the electron and ion densities are immediately in front of the electrodes, and the electron current density on the axis increases exponentially with distance from the cathode.

Points $a2$ and $a3$ are in the transition region between the Townsend and the normal regimes. Compared to point $a1$, the charged particle densities for point $a2$ are higher and the maximum in the ion density distribution is shifted towards the anode. The ion density reaches about 10^8 cm^{-3}, two orders of magnitude larger than the maximum electron density. The distortion of the external field by the ion space charge is quite small and the cathode sheath is not yet fully developed. The steady-state potential, ionization source term, and charged particle density distributions for point $a3$ are shown in the first panels of Figs. 4(a), 4(b), 5(a), and 5(b), respectively. Here the maxima in the steady-state electron and ion densities and in the ionization source term appear between the electrodes and the field is high on the axis in front of the cathode. The electron and ion densities are both on the order of 10^8 cm^{-3}, but the electron density is still lower than the ion density throughout the discharge volume. The radial field acts to spread the ion density over the volume and to focus the electrons towards the discharge axis. The maximum potential is slightly higher than the anode potential, and the field reverses sign in the vicinity of the axis at points near the anode. (The Townsend and subnormal discharges are discussed in more detail in Refs. [23] and [24].)

The spatial dependencies of the charged particle densities, axial component of the electric field, and ionization source term on the discharge axis for point $a3$ are shown in Fig. 6(a). The reason for the negative slope of the V-I characteristic in this region is that at a constant voltage and over the range of conditions of interest, the electron multiplication M (the integral of the ionization source term over the volume) increases when the space charge distortion of the field increases. Thus a higher current discharge in this regime requires a lower voltage to be self-sustained. (We have made no attempt here to investigate the current oscillations or instabilities in the transition from the Townsend to the subnormal discharge regime as studied recently [23].)

With further increases in the discharge current, a plasma (a region of $n_e \cong n_i$) forms first near the anode and then expands into the volume pushing the axial field to-

TABLE II. Calculated properties of steady-state discharges along the current-voltage characteristic B in Fig. 1 ($p=3$ torr). I is the discharge current, V_a is the anode potential, E_c is the axial field on the cathode, d_c is the sheath length on the axis, x_r is the axial position of the first field reversal, d_{ng} is the distance between the first and the second field reversals on the axis, V_{ng} is the depth of the negative glow region, M is the multiplication, and $n_{e(p)}$ is the maximal electron (positive ion) density.

	$p=3$ torr									
	I (μA)	V_a (V)	E_c (V/cm)	d_c (cm)	x_r (cm)	d_{ng} (cm)	V_{ng} (V)	M	n_e (cm^{-3})	n_p (cm^{-3})
$b3$	9.33	156.0	395	0.70				16.0	3.8×10^7	4.8×10^8
$b4$	64.1	132.3	1206	0.19	0.42	0.23	0.1	16.4	6.5×10^9	
$b5$	344.2	131.1	1450	0.16	0.24	0.29	0.34	16.6	1.1×10^{10}	
$b6$	5399	146.0	2994	0.09	0.14	0.37	0.39	16.9	6×10^{10}	

wards the cathode and the radial field towards the dielectric walls. It is a characteristic of glow discharges that there exists a range of currents for which the axial field in the center of the discharge is (almost) constant and the further expansion of the plasma over this range of current is in the radial direction. Discharges in this current range are termed "normal" glow discharges.

Normal glow discharges at two different currents (points *a*4 and *a*5) are illustrated in the second and third panels of Figs. 4(a), 4(b), 5(a), and 5(b) as indicated. It is seen in these figures and in Figs. 6(b) and 6(c) that the discharge properties on the axis change only slightly with increasing discharge current for these two points, and the increasing current is achieved rather by an increasing discharge area on the cathode surface. The voltage increases very slightly between points *a*4 and *a*5 (see Table I), and the calculated current densities at the axis on the cathode for these two points increase by a factor of 1.3. The ion density in the sheath is somewhat larger than the plasma density on the anode side of the volume. The plasma potential is slightly higher than the anode potential; a field reversal exists in a region around the discharge axis, at the end of the negative glow, and the position of the field reversal moves towards the cathode with increasing discharge current.

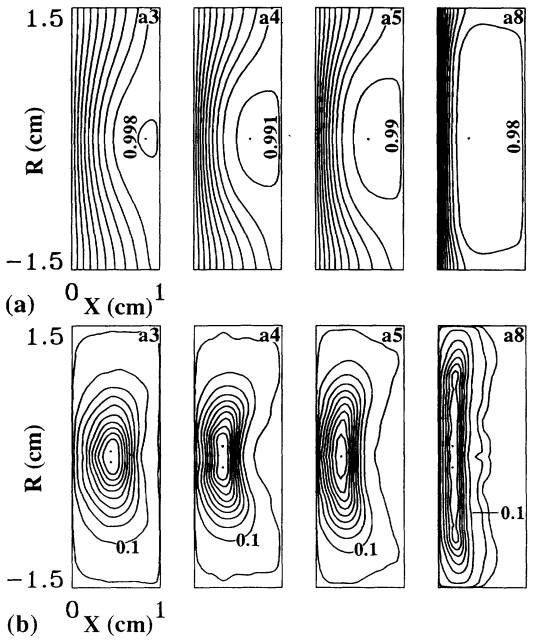

FIG. 4. (a) Contours of constant potential for the four points *a*3, *a*4, *a*5, and *a*8, as indicated along the characteristic *A* in Fig. 1 normalized to the maximum potential (127.2 V for *a*3, 123.9 V for *a*4, 127.5 V for *a*5, and 144.1 V for *a*8). Ten equally spaced contours are shown in each panel. (b) Contours of constant ionization source term for the four points *a*3, *a*4, *a*5, and *a*8, as indicated along the characteristic *A* in Fig. 1 normalized to the maximum ionization source term (2×10^{14} cm^{-3}s^{-1} for *a*3, 4.4×10^{14} cm^{-3}s^{-1} for *a*4, 6.1×10^{14} cm^{-3}s^{-1} for *a*5, and 3.7×10^{15} cm^{-3}s^{-1} for *a*8). The displayed contours are linear between 1.0 and 0.1 and thereafter decrease by factors of 10 per contour.

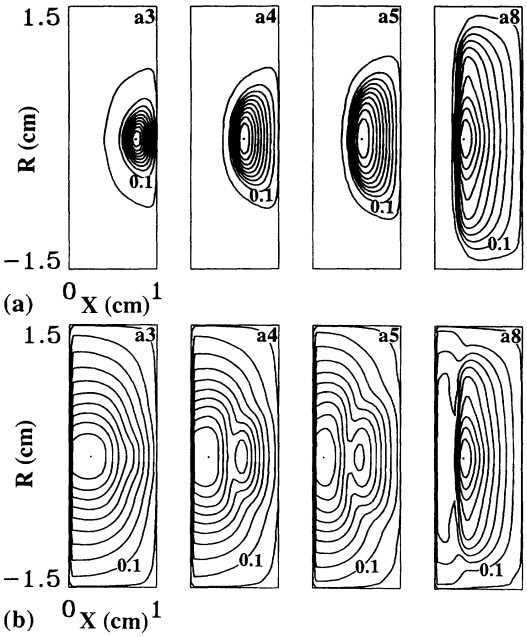

FIG. 5. (a) Contours of constant electron density for the four points *a*3, *a*4, *a*5, and *a*8, as indicated along the characteristic *A* in Fig. 1 normalized to the maximum electron density (1.4×10^{8} cm^{-3} for *a*3, 5.2×10^{8} cm^{-3} for *a*4, 6.6×10^{8} cm^{-3} for *a*5, and 8.2×10^{9} cm^{-3} for *a*8). The displayed contours are linear between 1.0 and 0.1 and thereafter decrease by factors of 10 per contour. (b) Contours of constant ion density for the four points *a*3, *a*4, *a*5, and *a*8, as indicated along the characteristic *A* in Fig. 1 normalized to the maximum ion density (4.7×10^{8} cm^{-3} for *a*3, 7.4×10^{8} cm^{-3} for *a*4, 9.5×10^{8} cm^{-3} for *a*5, and 8.2×10^{9} cm^{-3} for *a*8). The displayed contours are linear between 1.0 and 0.1 and thereafter decrease by factors of 10 per contour.

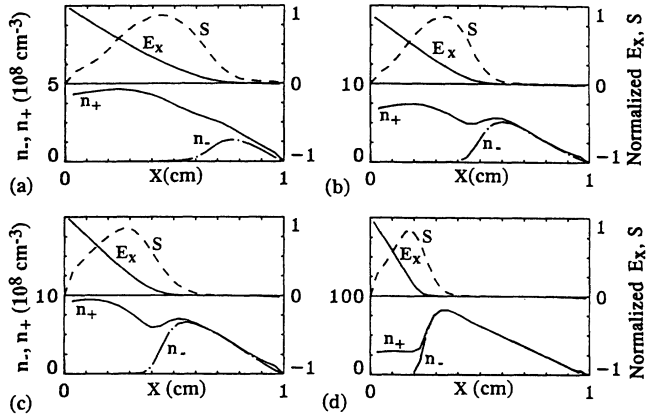

FIG. 6. Spatial dependence of the electron and positive ion densities, axial component of the electric field, and ionization source term on the discharge axis for four points along the *V-I* characteristic for 1 torr: (a) *a*3 (units 400 V cm^{-1} and 2.2×10^{14} cm^{-3}s^{-1} for the axial field and ionization source term, respectively); (b) *a*4 (units 600 V cm^{-1} and 5×10^{14} cm^{-3}s^{-1}); (c) *a*5 (units 600 V cm^{-1} and 7.1×10^{14} cm^{-3}s^{-1}); and (d) *a*8 (units 1200 V cm^{-1} and 4.3×10^{15} cm^{-3}s^{-1}).

As the discharge current continues to increase, the plasma expands further into the discharge volume and pushes the radial field toward the dielectric wall. Eventually, the entire cathode surface is surrounded by the plasma, and no further radial expansion is possible. It is only after the limit on its radial expansion has been reached that the plasma then expands in the axial direction, and the sheath length correspondingly decreases. From this point, further increases in the current require an increasing voltage, and discharges in this range of positive *V-I* are termed "abnormal" glow discharges.

The last panels in Figs. 4(a), 4(b), 5(a), and 5(b) illustrate an abnormal glow discharge and correspond to point *a*8 of the *V-I* characteristic. In contrast to the lower current points, the ion density in the plasma is greater than the ion density in the sheath. It can be seen that the entire surface of the cathode is covered by the discharge; the sheath length is markedly less than for the normal glow discharges, and the sheath length for the higher current point *a*9 is yet smaller. The radial distribution of the potential, the charged particle densities, and the ionization source term for point *a*9 are nearly uniform radially and the discharge is essentially one dimensional. Comparisons of 1D and 2D calculations of abnormal glow discharges under similar conditions confirm that the solutions on the axis are identical [25].

2. *Results for 3 torr*

In this section we describe points along the characteristic *B* in Fig. 1 corresponding to an argon pressure of 3 torr ($pd=3$ torr cm). The conditions are otherwise similar to those just discussed above. Figures 7 and 8 show the 2D distributions of the potential, the charged particle densities and the ionization source term for these 3-torr results.

The two, low current points *b*1 and *b*2 correspond to the Townsend regime. As above for the 1 torr calculations, the ion density is several orders of magnitude greater than the electron density, but the space charge is not sufficient to distort significantly the geometrical field distribution. The potential, charged particle densities, and ionization source term for point *b*3 of the characteristic *B* are illustrated in the first panels of Figs. 7(a), 7(b), 8(a), and 8(b). A plasma has started to form near the anode, but the ion density in the sheath is still many times higher than the plasma density. The distortion of the geometric field near the axis is the beginning of a

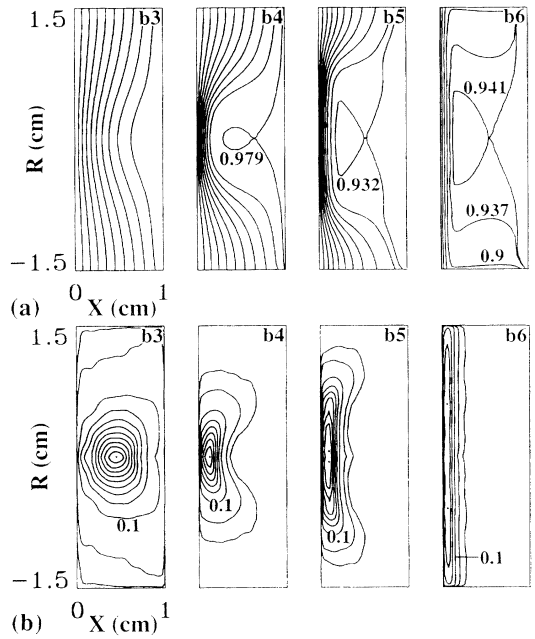

FIG. 7. (a) Contours of constant potential for the four points *b*3, *b*4, *b*5, and *b*6, as indicated along the characteristic *B* in Fig. 1 normalized to the maximum potential (158.4 V for *b*3, 129.3 V for *b*4, 132.7 V for *b*5, and 146 V for *b*6). Ten equally spaced contours are shown in each panel. (b) Contours of constant ionization source term for the four points *b*3, *b*4, *b*5, and *b*6, as indicated along the characteristic *B* in Fig. 1 normalized to the maximum ionization source term (1.3×10^{14} cm^{-3}s^{-1} for *b*3, 4.3×10^{15} cm^{-3}s^{-1} for *b*4, 8.1×10^{15} cm^{-3}s^{-1} for *b*5, and 6.3×10^{16} cm^{-3}s^{-1} for *b*6). The displayed contours are linear between 1.0 and 0.1 and thereafter decrease by factors of 10 per contour.

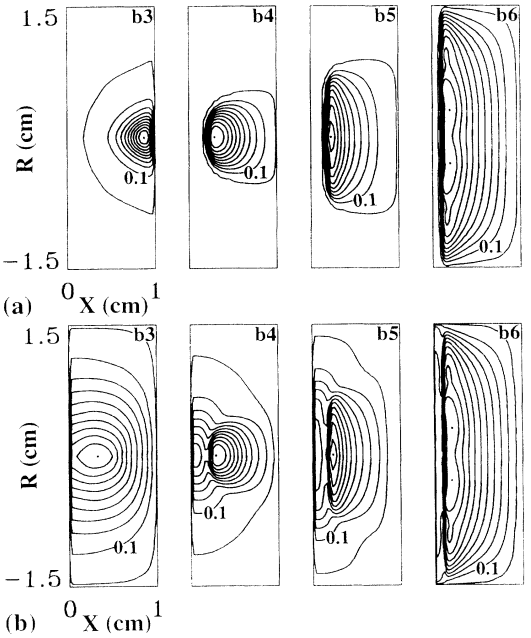

FIG. 8. (a) Contours of constant electron density for the four points *b*3, *b*4, *b*5, and *b*6, as indicated along the characteristic *B* in Fig. 1 normalized to the maximum electron density (3.8×10^{7} cm^{-3} for *b*3, 6.5×10^{9} cm^{-3} for *b*4, 1.1×10^{10} cm^{-3} for *b*5, and 6×10^{10} cm^{-3} for *b*6). The displayed contours are linear between 1.0 and 0.1 and thereafter decrease by factors of 10 per contour. (b) Contours of constant ion density for the four points *b*3, *b*4, *b*5, and *b*6, as indicated along the characteristic *B* in Fig. 1 normalized to the maximum ion density (4.8×10^{8} cm^{-3} for *b*3, 6.5×10^{9} cm^{-3} for *b*4, 1.1×10^{10} cm^{-3} for *b*5 and 6×10^{10} cm^{-3} for *b*6). The displayed contours are linear between 1.0 and 0.1 and therefore decrease by factors of 10 per contour.

cathode sheath.

Points *b*4 and *b*5 of the characteristic *B* are in the normal glow regime. The discharge current increases by a factor of 50 between points *b*4 and *b*5, which the current densities at the cathode on the axis changes by a factor of 1.6. The increase in the current is thus due to the increase in the cross sectional area of the plasma in front of the cathode. The voltage changes very slightly between points *b*4 and *b*5. These properties are seen in the second and third panels of Figs. 7(a), 7(b), 8(a), and 8(b) as indicated. Compared to the 1 torr normal glow regime, the plasma boundary in these 3 torr results is sharper due to the reduced diffusion at the higher pressure, and the radial fields are consequently higher. The radial field for point *b*4 reaches a maximum of 170 V/cm, three times the maximum of the radial field observed at 1 torr in the normal regime. (Note that our assumption of a constant D_-/μ_- will influence somewhat the quantitative results here but not the overall trends.) In these 3 torr results, the field along the axis is seen to change sign twice, and the maximum potential in the gap is the anode potential. The position of the second field reversal marks the end of the negative glow. In contrast, at 1 torr, we found one field reversal and a plasma potential greater than the anode potential.

Point *b*6 is an abnormal discharge. As seen in the last panels of Figs. 7(a), 7(b), 8(a), and 8(b), the whole surface of the cathode is covered by the discharge and the luminous intensity, which is approximately proportional to the ionization source term, is correspondingly predicted to be uniformly distributed all over the cathode surface. The sheath length is about half of that for points *b*4 and *b*5, and the discharge is almost one dimensional.

B. Transition to a positive column

In discharges which are long with respect to the length of the cathode region, a positive column is needed to complete the circuit. In this region, an electric field must exist in order to accelerate the low energy electrons from the negative glow and to provide enough ionization to balance the charged particle losses to the walls or through recombination. The region between the negative glow and the positive column is the Faraday dark space, the length of which depends on the radial loss of charged particles. In this section we present results from the calculation in which the transition to a positive column is clearly seen. The background gas (argon) pressure is 1.1 torr, the potential of the generator is 400 V, and the resistor of the external circuit R is 10^5 Ω. The discharge length is 3 cm and the discharge and electrode diameter is 1 cm.

The steady-state discharge current and voltage predicted from this calculation are shown as point *pc*1 in Fig. 1. This discharge is long enough for a distinct positive column region to appear in the model calculation. Some of the discharge properties for this calculation are compiled in Table III. The potential distribution and contours of constant electron density and ionization source term are shown in Fig. 9. The axial distributions of the electron and ion densities, the ionization source term, and the axial component of the electric field are shown in Fig. 10(a). The cathodic regions, the Faraday dark space, the positive column, and the anodic region appear clearly in these figures.

The behavior of the cathode regions in this longer discharge is quite the same as for the shorter abnormal discharges described above. The axial electric field decreases almost linearly in the cathode fall, and the sheath length is slightly larger for radial positions closer to the wall. The radial electric field acts to extract ions from the discharge over most of the volume of the discharge tube. The wall charge density is negative and constant in the positive column.

There is a field reversal in the negative glow which extends over the whole discharge radius, and the position of the field reversal does not change much with radial position. A potential barrier thus inhibits the ions created on the anode side of the field reversal from reaching the cathode. The region delimited by the cathode, the walls and the line of axial field reversal is self-sustained [19,20], i.e., the electron multiplication in this region is equal to $1+1/\gamma$ ($=15.3$). The electron current through the surface delimited by the locus of axial field reversals is exactly equal to the discharge current. A second field reversal can be seen at the end of the negative glow so that electrons can be accelerated toward the anode side of the discharge.

The 2D spatial distribution of the ionization source term is shown in Fig. 9(c). For all radial positions, the ionization source term is a maximum at the cathode sheath boundary and decreases to zero in the Faraday dark space at the end of the negative glow because the electrons no longer have enough energy to produce ionization. There is a slight maximum in the axial field at the end of the Faraday dark space; Druyvesteyn and Pen-

TABLE III. Calculated properties of the steady-state discharge with a positive column, *pc*1, in Fig. 1 ($p=1.1$ torr). I is the discharge current, V_a is the anode potential, E_c is the axial field on the cathode, d_c is the sheath length on the axis, x_r is the axial position of the first field reversal, d_{ng} is the distance between the first and the second field reversals on the axis, V_{ng} is the depth of the negative glow region, M is the multiplication, and $n_{\text{glow (column)}}$ is the maximal plasma density in the negative glow and positive column, respectively.

	$p=1.1$ torr									
	I (μA)	V_a (V)	E_c (V/cm)	d_c (cm)	x_r (cm)	d_{ng} (cm)	V_{ng} (V)	M	n_{glow} (cm^{-3})	n_{column} (cm^{-3})
*pc*1	870	312.2	3826	0.12	0.24	0.72	2.0	21.1	2.9×10^{11}	6.5×10^{9}

ning, in their review article [26], mention that there are "experimental indications of the existence of this maximum." The field increases past the dark space to pull the cooled electrons towards the anode, and the ionization source term increases correspondingly. The field in the positive column adjusts so that electron losses to the walls are exactly balanced by volume ionization. The ionization source term increases again in the increasing field in the anode fall. The field increase in this region is due to the electron space charge (the ion flux from the anode is zero).

Figure 10(b) shows radial profiles of the electron and ion densities and potential in the positive column (1.8 cm from the cathode). There is a positive ion sheath around the dielectric wall which is established so that the net flux of charged particles to the wall is zero. The potential difference between the axis of the discharge and the wall increases slightly toward the cathode and decreases slightly toward the anode. It should be emphasized that the radial field acts only to confine the electrons in the column and has practically no influence on the electron power balance in the discharge since there is no net acceleration of the electrons in the radial field (except for the few electrons born in the wall sheath region).

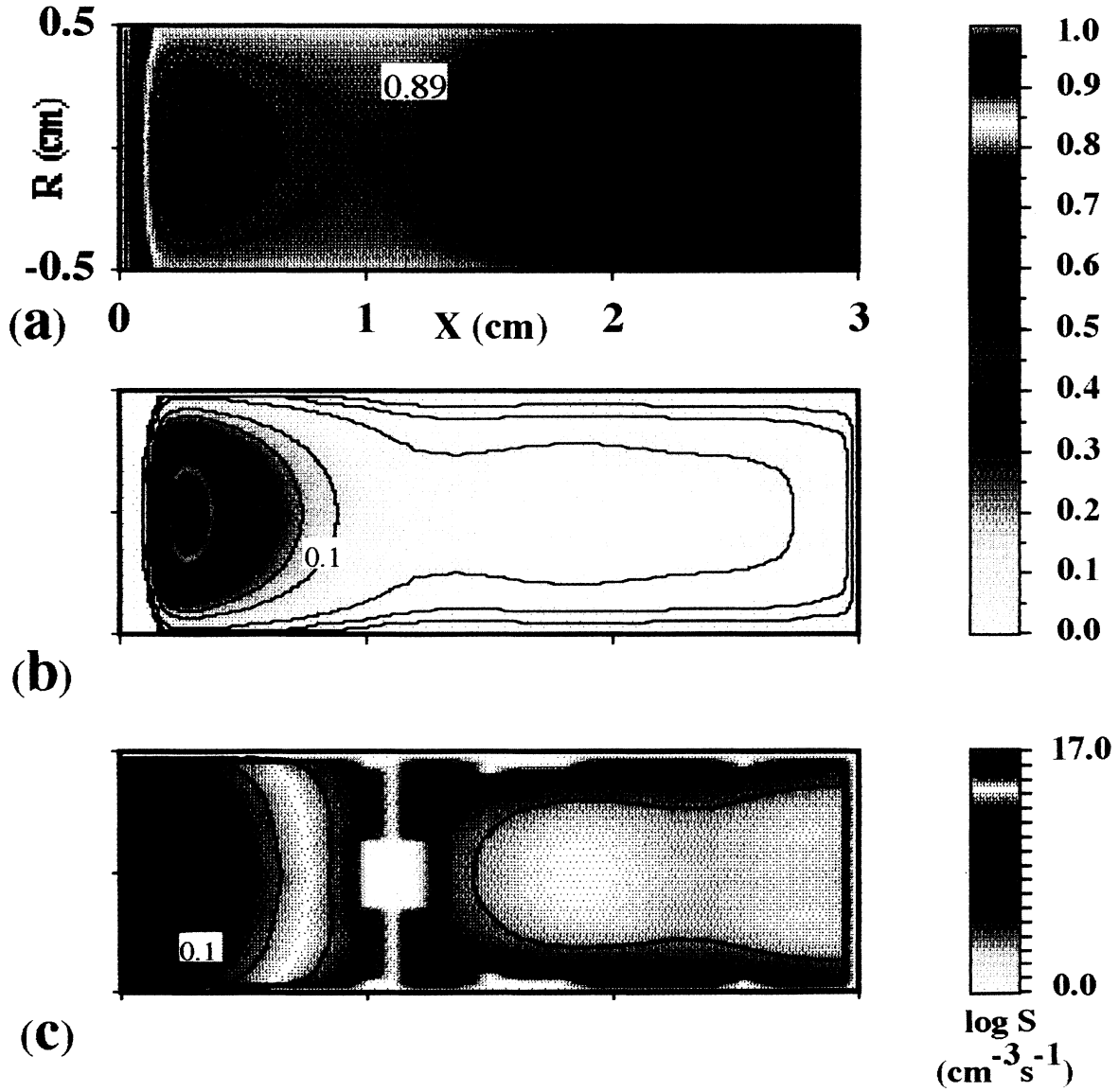

FIG. 9. (a) Contours of constant potential for the positive column point *pc*1 of Fig. 1 in units of 309.7 V; (b) contours of constant electron density for the positive column point *pc*1 in units of 2.9×10^{11} cm^{-3}; (c) contours of constant ionization source term for the positive column point *pc*1 in units of 8.5×10^{16} cm^{-3} sec^{-1}. The contours indicated by the solid lines are equally spaced for the potential and, for the density and source term, the contours are linear between 1.0 and 0.1 and thereafter decrease by factors of 10 per contour.

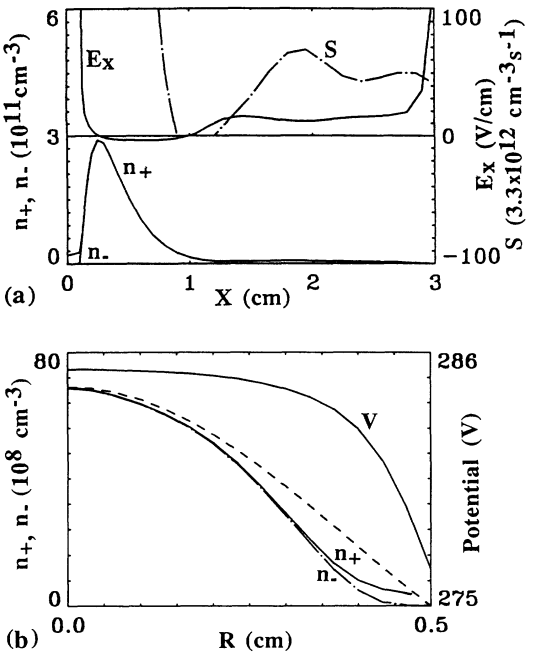

FIG. 10. (a) Spatial dependence of the electron and positive ion densities, axial component of the electric field and ionization source term on the discharge axis for the positive column point *pc*1. (b) Radial profiles of the electron density, ion density and potential for the positive column point *pc*1 at a position $x=1.8$ cm from the cathode. The dashed line shows the J_0 Bessel function profile.

IV. DISCUSSION OF RESULTS

In this section we return to a few of the points raised above.

A. Effects of nonlocal ionization

In the previous 2D models of dc glow discharges of Refs. [3] and [4], the ionization source term was assumed to be a function of the local value of the reduced field $E(\mathbf{r})/p$. This approach gives a reasonable prediction for the *V-I* characteristics and for the qualitative features of the transition from normal to abnormal discharges. The global discharge behavior is correctly predicted with the local field approximation because it is the total number of ionization events in the volume rather than the details of their spatial distribution which control these properties. However, as has been emphasized in recent 1D calculations [5,28,29], the spatial distribution of ionization events cannot be predicted by the local field approximation (except in the positive column of a long discharge). Thus, local ionization models such as those presented in Refs. [3] and [4] cannot predict qualitatively the existence of the negative glow.

The main distinction between the model presented here and the previously published 2D models is that the ionization source term in the present model is determined from a kinetic calculation. This distinction is essential to the negative glow which can be considered as an externally sustained plasma; that is, the glow is sustained by the high energy electrons generated in the cathode fall and accelerated through the sheath (see the discussion on the electron energy distributions below). The maximum extent of the negative glow is nearly equal to the range of electrons, with an energy equivalent to the cathode fall voltage, in a zero field [20]. The calculations presented here, although subject to the approximation of constant average energy for the bulk electrons (see below), are expected to be quite accurate in the cathode regions and they thus provide points for comparison (sheath length, length of negative glow, position of field reversal, etc.) with other simpler numerical or analytical models.

B. Axial field reversals in the negative glow

We turn now to the question of the field reversal on the axis which appears in our calculations for all normal and abnormal discharges, and in this discussion we follow the argument of Raizer [2]. Although the details of the field reversal depend to some extent on our assumption of a constant electron energy equal to 1 eV, several general conclusions can be drawn.

During the transition from a subnormal to a normal discharge, a plasma appears first on the axis near the anode and then spreads towards the cathode and the side walls as the discharge current increases. The current density $\mathbf{j}$ at any point in a quasi-neutral plasma of density n is

$$\mathbf{j}=\mathbf{j}_+ +\mathbf{j}_- =e(D_- -D_+)\nabla n +e\mathbf{E}(\mu_- +\mu_+)n \ . \quad (9)$$

Thus the electric field is given by

$$\mathbf{E}=\frac{\mathbf{j}}{e(\mu_- +\mu_+)n}-\frac{(D_- -D_+)}{(\mu_- +\mu_+)}\frac{\nabla n}{n}, \quad (10)$$

which is a sum of two terms, the first depending on the total current and the local conductivity and the second being an ambipolar field due to the density gradients.

In a region of large plasma density gradient the total field may tend to zero or even reverse in direction with respect to the current, in which case the electron diffusion current dominates the electron drift current. This situation of field reversal can occur in the negative glow where the large plasma density gradient is induced by the nonlocal ionization. The ambipolar field which results on the anode side of the density maximum in the negative glow tends to confine the electrons inside the negative glow and to accelerate the ions towards the anode (and the walls).

Our calculations are in agreement with the arguments above. The locus of axial field reversals can be easily deduced from the equipotential contours of Figs. 4(a), 7(a), and 9(a), and corresponds to the points where the tangent to an equipotential curve is parallel to the discharge axis. We find that the position of the first reversal in the field moves from the anode towards the cathode as the discharge current increases, as can be seen in Tables I and II. For a discharge without positive column [see Fig. 4(a)], the field can remain negative (such as to push electrons towards the cathode) from the point of the field reversal to the anode. The maximum potential in the plasma is, in that case, higher than the anode potential, and positive ions are lost on the anode. When a positive

column exists [see Fig. 9(a)], or for a discharge with a long enough pressure-gap length product [see Fig. 7(a)], the electric field direction can reverse a second time, such as to push electrons towards the anode after the second field reversal. Note that, in the normal discharge of Fig. 7(a), cases *b*4 and *b*5, there is no loss of positive ions at the anode, and the positive ions created in the region of axial field reversal return to the cathode along the field lines, i.e., they are first directed toward the anode and radially outward toward the walls, and then they are "turned back" to the cathode. In the abnormal discharge of Fig. 7(a), case *b*6, and in the discharge with positive column of Fig. 9(a), the positive ions created in the region of field reversal are lost to the walls.

In models where the ionization rate coefficient is assumed to depend on the local value of the electric field, the plasma density gradient along the discharge axis is never large enough to induce a reversal of the axial field. Note that the existence of axial field reversals in the negative glow of dc discharges has been observed experimentally by Gottscho *et al.* [27] and has also been shown with 1D self-consistent discharge models [5,28–31]. The effect of our assumed constant value of the electron characteristic energy on the field reversal is discussed in subsection E.

C. Axial dependence of the electron energy distribution function

The evolution of the (radially integrated) electron energy distribution function (EEDF) with axial position is illustrated in Fig. 11. Here we show the EEDF's calculated from a Monte Carlo simulation in the steady-state electric field configuration for point *pc*1 at the three different axial positions equal to 0.2, 1, and 2 cm from the cathode [see Fig. 10(a)]. The high energy tail of the EEDF near the end of the cathode fall and entering the negative glow (at $x=0.2$ cm) extends to the total energy available, $eV(d_c)$, where $V(d_c)$ is the total potential drop in the cathode fall, and at the end of the negative glow ($x=1$ cm), there are essentially no electrons in the simulated distribution with an energy greater than the ionization potential. A comparison of these two distribution functions illustrates dramatically the fact that the negative glow is a discharge sustained externally by the energetic electrons entering from the cathode fall.

The EEDF at $x=2$ cm, a position 11 V downstream from the end of the negative glow and well into the region of constant and positive electric field ($E/p \sim 12$ V cm^{-1} torr^{-1}), is also shown in Fig. 11(b) (dashed-dot line). The local field EEDF at 12 V cm^{-1} torr^{-1} is included in Fig. 11(b) for comparison. The EEDF predicted from the Monte Carlo simulation appears to be deficient in electrons of energies from about 5 to 15 eV and to have a slightly higher tail, but the statistical accuracy is not sufficient to draw more detailed conclusions. The average electron energy predicted from this local field EEDF is 5.6 eV. Our assumed value of the electron average energy (1 eV) in the fluid equations is questionable when the local field average energy is predicted to be 5.6 eV, and we return briefly to this point below.

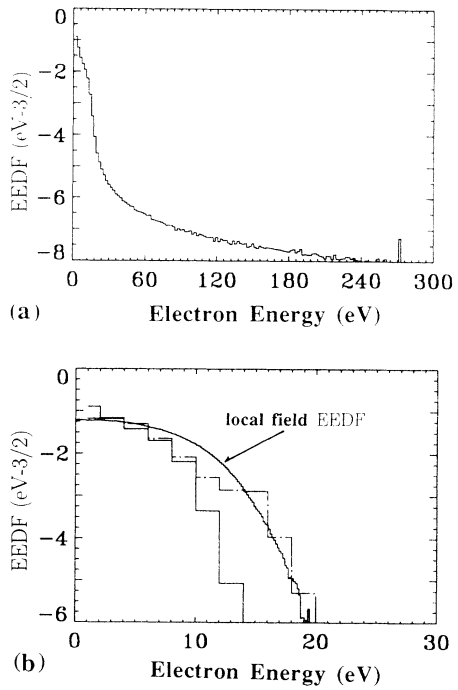

FIG. 11. (a) Electron energy distribution function (log scale) integrated over the discharge radius at a position $x=0.2$ cm from the cathode. (b) Electron energy distribution function (log scale) integrated over the discharge radius at $x=1$ cm (full line) and $x=2$ cm (dashed-dot line) from the cathode and compared to the local field energy distribution function for $E/p=11$ V cm^{-1} torr^{-1} (the calculated value of E/p near the axis).

D. Positive column field

Estimates of the field in the positive column are often deduced from the 1D (in the radial direction) continuity equation for electrons or ions in which ambipolar diffusion and recombination or attachment losses are balanced by the ionization. Since the ionization and the losses depend on the value of the electric field, the conditions of the local particle balance determines the electric field. For a positive column where radial ambipolar diffusion to the walls is the dominant charged particle loss, one can show [2,19,20] (assuming that the axial field does not change with radial position) that the axial field in the plasma adjusts so that the following equation be satisfied

$$\nu_i = D_a (2.405/R)^2 , \tag{11}$$

where ν_i is the ionization frequency, D_a is the ambipolar diffusion coefficient, and R is the tube radius. Since ν_i and D_a are functions of E/p in an equilibrium positive column, the electric field can be deduced from the above equation.

For our conditions, application of this simple model using values of the ionization rate consistent with the EEDF's determined from a solution of the Boltzmann equation and using the cross sections of Fig. 3 yields a field of about 9.5 V cm^{-1} in the positive column (assuming a uniform field, a 1 cm diameter, and a pressure of 1.1

torr). Although the positive column is not long enough to state conclusively that the EEDF is in local equilibrium with the field, this simple estimate of the field in the column reasonable agrees with the results of the 2D model which give a field of 12 V cm^{-1} on the axis.

When the diffusion losses to the wall dominate the recombination losses, the solution of the radial ambipolar diffusion equation for the charged particle densities is a Bessel radial profile [19]. A Bessel radial profile is shown by the dashed line in Fig. 10(b) for comparison with calculations from the 2D model (solid line). The rather large differences for the 1-cm diameter tube are probably due to the radial dependence of the calculated axial field which is not included in the 1D picture, and the Bessel radial profile is more representative of distributions from other of our calculations (not shown) in wider diameter discharge tubes where the axial field is less dependent on the radial position. The radial profile of the electron density has recently been measured [32] in the positive column of helium and of neon discharges under conditions of pressure and cathode current density close to those reported here for argon. The measured density profiles show a departure from a Bessel profile similar to that seen in Fig. 10(b).

E. Evaluation of approximations and precision of numerical results

There are several approximations which were made in the model presented above. Perhaps the most questionable of these is the assumption of a constant characteristic electron energy, $D_-/\mu_- = 1$ eV, for the bulk electrons. We choose to impose this condition rather than to solve the electron energy equation with its attendant numerical complexity. Furthermore, electron-electron collisions, superelastic collisions, and stepwise ionization can also play an important role in the electron energy balance in the glow [31]. Since it was beyond the scope of this paper to include these processes, we chose to consider D_-/μ_- as a parameter. One calculation was performed for discharge conditions similar to the point *pc*1 but with D_-/μ_- taken to be 5 eV instead of 1 eV (*pc*1). Not surprisingly, we find that the features of the discharge which are most sensitive to the assumed value for the average energy are the depth of the negative glow and the wall sheath potential in the positive column. The precise position of the field reversal in the direction parallel to the discharge axis depends only weakly on the value of D_-/μ_-. The value of the difference between the local maximum of potential associated with the field reversal and the anode potential (or the potential at the second field reversal if any) is however strongly related to the value of D_-/μ_-, since a net electron current must flow towards the anode (this potential difference cannot be much larger than the electron mean energy). The voltage drop in the wall sheath in the positive column increases from 9 eV for $D_-/\mu_- = 1$ eV to 45 eV for $D_-/\mu_- = 5$ eV.

In all these calculations, the gas temperature was assumed to be constant and equal to 273 K. Estimates of the importance of gas heating have been made for the highest current points along the characteristics *A* and *B*, and the maximum gas temperature which would result from the discharge conditions presented above is 294 K for point *a*9 if the electrodes are assumed to be kept at a constant 273 K. Neglect of the gas temperature is therefore justified over the range of discharge currents presented here. We have also made calculations at higher discharge currents, but since the estimated maximum gas temperature rapidly increases with increasing current, the effect of the gas temperature can no longer be neglected. Self-consistent calculations including the effect of an increasing gas temperature for higher current density discharges [12] will be published separately.

We have further neglected the buildup of excited state densities which could enhance the ionization through collisions between metastables and superelastic collisions. These effects are increasingly more important as the pressure increases [33].

The secondary electron emission is assumed to be due to ion impact with a secondary electron emission constant and equal to 0.07. Photons and metastables also induce secondary emission, but, at steady state, the ratio of the photoemission and metastable induced emission to the ion induced emission is constant. The value of γ is therefore to be considered as an effective value which includes photon and metastable effects as well as ion induced secondary emission.

Finally, the statistical nature of the Monte Carlo simulation results in small fluctuations of all physical variables in the steady state. The values of the current and potential, the axial field on the cathode, and the multiplication and the maximal densities of the charged particles from Tables I, II, and III are averaged over hundreds of time steps after reaching the steady state, while the sheath length, positions of the field reversal, and the depth of the negative region are represented by their last instantaneous values. It should be underlined that these small fluctuations do not change the physical picture and can be controlled (they represent less than 3% of the average value in our calculations).

V. SUMMARY

We have presented results from a 2D, hybrid fluid-particle model of dc glow discharges in a cylindrical geometry. The aim of this work was not to study the particular set of experimental conditions but rather to provide a full set of calculations for typical low-pressure discharge conditions using a realistic description of the ionization source term. Two-dimensional profiles of the charged particle density and potential distributions are presented along with the ionization source term for conditions chosen to illustrate the transition from a normal to an abnormal discharge and for longer discharges where a transition to a positive column is apparent. The inclusion of a nonlocal ionization source term in the model yields an accurate description of the negative glow, the regions of the field reversal, and details of the transition to a positive column.

This model has also been applied to more complicated hollow cathode [10] and rod-rod [12] electrode

geometries and in the calculation of the transient development of discharges in plane-plane and other more complex geometries. Our results in nonplanar geometries and for the transients will be published separately.

ACKNOWLEDGMENTS

We would like to thank Dr. A. V. Phelps for a series of useful discussions and for his comments on the manuscript. The Centre de Physique Atomique is "Unité de Recherche Associée du CNRS No. 277.

APPENDIX: NUMERICAL SOLUTIONS OF THE FLUID-POISSON EQUATIONS

We define a two-dimensional, axisymmetric grid (x_i, r_j) where $i=1,nx$ and $j=1,nr$. The spacing between two successive grid points is equal to $\Delta x_i = x_{i+1} - x_i$, $i=1,nx-1$, and $\Delta r_j = r_{j+1} - r_j$, $j=1,nr-1$ for axial and radial directions, respectively. We further introduce the distance between midpoints of the grid: $dx_i = (\Delta x_{i-1} + \Delta x_i)/2$ for $i=2,\ldots,nx-1$ and $dx_{nx} = \Delta x_{nx-1}/2$, $dx_1 = \Delta x_1/2$. The fundamental variables, the electron density, the ion density and the potential, denoted n^k_{-ij}, n^k_{+ij}, and V^k_{ij} at time t^k, are defined on the grid points (x_i, r_j). The fluxes and the electric field are defined at the midpoints $i\pm\frac{1}{2}$, $j\pm\frac{1}{2}$, e.g., $\phi^k_{r\,i,j\pm1/2}$ or $\phi^k_{x\,i\pm1/2,j}$ for the radial and axial components of either the electron or the ion flux, and similarly for the field.

The continuity equations (1) and (2) are expressed in the following discrete form using a Crank-Nicolson estimate of the time derivatives,

$$\frac{n^{k+1}_{ij} - n^k_{ij}}{\Delta t} + \tfrac{1}{2}[(\nabla_r \phi_r)^{k+1}_{ij} + (\nabla_r \phi_r)^k_{ij}] + \tfrac{1}{2}[(\nabla_x \phi_x)^{k+1}_{ij} + (\nabla_x \phi_x)^k_{ij}] = S^k_{ij} \ , \quad \text{(A1)}$$

where

$$\nabla_r Y = \frac{1}{r}\frac{\partial}{\partial r}(rY)$$

and

$$\nabla_x Y = \frac{\partial}{\partial x}(Y) \ ,$$

and Poisson's equation in the form

$$\Delta V = -\frac{e}{\varepsilon_0}(n_+ - n_-) \quad \text{(A2)}$$

is discretized as

$$(\nabla_r E_r)^{k+1}_{ij} + (\nabla_x E_x)^{k+1}_{ij} = \frac{e}{\varepsilon_0}(n_+ - n_-)^{k+1}_{ij} \ , \quad \text{(A3)}$$

where $E_{r(x)}$ is the radial (axial) component of the electric field. The discretization of the radial gradients of ϕ and E in Eqs. (A1) and (A3) requires special attention because of the singularity on the axis. A convenient discrete representation follows from the Green's theorem which relates the integral of the divergence of ϕ over a volume element δV to the integral of the surface flux into that volume element

$$\nabla_r \phi_r = \frac{1}{\delta V}\int_S (\phi_r)_n dS \ , \quad \text{(A4)}$$

where $(\phi_r)_n$ denotes the component of the flux normal to the surface element dS. The discretization of the radial gradient for points $r>0$ off the axis ($j>1$) is then

$$(\nabla_r \phi_r)^k_{ij} = \frac{1}{\delta V_{ij}}\{\phi^k_{r_{i,j+1/2}} \delta S_{i,j+1/2} - \phi^k_{r_{i,j-1/2}} \delta S_{i,j-1/2}\} \ , \quad \text{(A5)}$$

where $\delta V_{ij} = \pi dx_i\{(r_j + \Delta r_j/2)^2 - (r_j - \Delta r_j/2)^2\}$, and the surface elements are $\delta S_{i,j+1/2} = 2\pi dx_i\{r_j + \Delta r_j/2\}$ and $\delta S_{i,j-1/2} = 2\pi dx_i\{r_j - \Delta r_{j-1}/2\}$. On the axis ($r=0, j=1$),

$$(\nabla_r \phi_r)^k_{i,1} = \frac{1}{\delta V_{i,1}}\phi^k_{r_{i,3/2}} \delta S_{i,3/2} \ , \quad \text{(A6)}$$

where $\delta V_{i,1} = \pi \Delta r_1^2 dx_i/4$ and $\delta S_{i,3/2} = \pi dx_i \Delta r_1$.

The heart of the discretization scheme is the representation of the flux which makes use of the exponential scheme proposed by Sharfetter and Gummel [8]. Assuming that the flux and the mobility and diffusion coefficients are constant between any two successive points on the grid, the momentum transfer Eq. (4) can be integrated analytically between these points to yield,

$$\phi_{x\,i+1/2,j} = \frac{1}{\Delta x_i}[n_{ij} D_{ij} \exp(z_{i+1/2,j}) - n_{i+1,j} D_{i+1,j}] \times \frac{z_{i+1/2,j}}{\exp(z_{i+1/2,j}) - 1} \ , \quad \text{(A7)}$$

where

$$z_{i+1/2,j} = -s\frac{\mu_{i+1/2,j}}{D_{i+1/2,j}}(V_{i+1,j} - V_{i,j}) \ , \quad \text{(A8)}$$

and D is the diffusion coefficient, μ is the mobility, and $s=+1$ for the positive ions and $s=-1$ for the electrons. Similar expressions can be obtained for $\phi_{x\,i-1/2,j}$ and $\phi_{r\,i,j\pm1/2}$.

This discretization provides a numerically stable estimation of the particle flux under all conditions. For a small difference of voltage between two successive grid points Eq. (A7) approaches the standard difference relation for the diffusion flux, and if the difference is large it approaches the drift flux.

To complete the discretization of Poisson's equation, we express the axial gradient of the field $(\partial E_x/\partial x)_{ij} = (E_{x\,i+1/2,j} - E_{x\,i-1/2,j})/dx_i$ and then express the field in terms of the potential at two neighboring grid points, e.g., $E_{r\,i,j+1/2} = -(V_{i,j+1} - V_{i,j})/\Delta r_j$ and $E_{x\,i+1/2,j} = -(V_{i+1,j} - V_{i,j})/\Delta x_i$ for the radial and axial components of the field, respectively.

Newton's iterations are used to solve the system of the discretized equations. We define the vector of the fundamental variables $\mathbf{X} = (n_e, n_p, V)$ and linearize the continuity equations by performing a Taylor series expansion keeping terms to first order $\mathbf{X}^{k+1} = \mathbf{X}^0 + \delta\mathbf{X}$, where δ's are increments of the fundamental variables with respect to their value at the last iteration. $\mathbf{X}^0$ is a trial value of

the function, which is taken to be its value from the previous Newton's iteration. The first Newton's iteration at t^{k+1} starts with the trial value $\mathbf{X}^0=\mathbf{X}^k$, the value at the last converged time. The linearization can be expressed, e.g., for the axial flux, as follows (index x has been omitted):

$$\begin{aligned}\phi^{k+1}_{i+1/2,j}&=\phi^k_{i+1/2,j}+\delta\phi_{i+1/2,j}\\&=\phi^k_{i+1/2,j}+\frac{\partial\phi_{i+1/2,j}}{\partial n_{ij}}\delta n_{ij}+\frac{\partial\phi_{i+1/2,j}}{\partial V_{ij}}\delta V_{ij}\\&\quad+\frac{\partial\phi_{i+1/2,j}}{\partial n_{i+1,j}}\delta n_{i+1,j}+\frac{\partial\phi_{i+1/2,j}}{\partial V_{i+1,j}}\delta V_{i+1,j}\ .\end{aligned}\tag{A9}$$

The test for convergence of the Newton iterations was a relative change in the fundamental variables of less than 10^{-4}. The statistical fluctuations in the Monte Carlo derived ionization source term influence very little convergence properties of the system; more important to the convergence is the fact that the ionization source term is nonlocal.

Poisson's equation is linear in itself but it has also been written in terms of the increments of the fundamental variables, $\delta\mathbf{X}$, to be consistent with the continuity equations. Thus Eqs. (1)–(3) can be expressed as relations between values of increments at three adjacent grid points in i and j and terms which depend on values of the fundamental variables and the ionization source term at the previous time k. These equations can be written in a matrix form as follows

$$\begin{aligned}&\mathbf{A}_{ij}\delta\mathbf{X}_{i-1,j}+\mathbf{B}_{ij}\delta\mathbf{X}_{ij}+\mathbf{C}_{ij}\delta\mathbf{X}_{i+1,j}\\&\qquad=\mathbf{D}_{ij}\delta\mathbf{X}_{i,j-1}+\mathbf{E}_{ij}\delta\mathbf{X}_{i,j+1}+\mathbf{F}^k_{ij}\ ,\end{aligned}\tag{A10}$$

where the matrices of the coefficients **A**, **B**, **C**, **D**, and **E** depend on the fundamental variables at the last Newton's iteration. The vector **F** depends on the source term and the fundamental variables at the time t^k.

A successive line over relaxation method is used to solve the matrix system (A10) for the increments $\delta\mathbf{X}$. Thus Gaussian elimination is used to invert the matrix for each of the j one-dimensional systems by assuming that the values of the variables on the lines $j-1$ and $j+1$ are known. Several iterations are necessary to find a converged solution to this two-dimensional system with a typical value of 1.5 taken for the overrelaxation parameter. The test for convergence of the matrix system was a change of less than 10^{-4} in the calculated values of the increments $\delta\mathbf{X}$. The same convergence criteria were applied for all cases reported here.

[1] G. G. Lister, J. Phys. D **25**, 1649 (1992).

[2] Y. P. Raizer, *Gas Discharge Physics* (Springer-Verlag, Berlin, 1991).

[3] J. P. Boeuf, J. Appl. Phys. **63**, 1342 (1988).

[4] P. Y. Raizer and S. T. Surzhikov, Teplofiz. Vys. Temp. **26**, 428 (1988) [High Temp. (USSR) **26**, 304 (1988)].

[5] M. Surendra, D. B. Graves, and G. M. Jellum, Phys. Rev. A **41**, 1112 (1990).

[6] J. E. Lawler, Phys. Rev. A **32**, 2977 (1985).

[7] M. Kurata, *Numerical Analysis for Semiconductor Devices* (Heath, Lexington, MA, 1982).

[8] D. L. Scharfetter and H. K. Gummel, IEEE Trans. Electron. Devices **ED-16**, 64 (1969).

[9] J. P. Boeuf and E. Marode, J. Phys. D **15**, 2169 (1982).

[10] J. P. Boeuf and L. C. Pitchford, IEEE Trans. Plasma Sci. **19**, 286 (1991).

[11] A. L. Ward, J. Appl. Phys. **33**, 2789 (1962).

[12] A. Fiala, L. C. Pitchford, and J. P. Boeuf, Bull. Am. Phys. Soc. **38**, 2358 (1993).

[13] This cross section set was assembled by M. C. Bordage and P. Segur (private communication, 1989) and is based on S. Hunter, X. Carter, and L. Christophorou, J. Chem. Phys. **90**, 4879 (1986) for the momentum transfer cross section, J. Bretagne, G. Callede, M. Legentil, and V. Puech, J. Phys. D **19**, 761 (1986) for the excitation cross sections, and D. Rapp and P. Englander-Golden, J. Chem. Phys. **43**, 1464 (1965) for the ionization cross section.

[14] E. A. Den Hartog, D. A. Doughty, and J. E. Lawler, Phys. Rev. A **38**, 2471 (1988).

[15] T. Holstein, Phys. Rev. **70**, 367 (1946).

[16] S. Yoshida, A. V. Phelps, and L. C. Pitchford, Phys. Rev. A **27**, 2858 (1983).

[17] C. B. Opal, W. K. Peterson, and E. C. Beaty, J. Chem. Phys. **55**, 4100 (1971).

[18] N. Ouadoudi, Thése de 3ème cycle, Université Paul Sabatier (1994).

[19] A. Von Engel, *Ionized Gases* (Oxford University Press, London, 1965).

[20] E. Badareu and I. Popescu, *Gaz Ionisés* (Editions Dunod, Paris, 1965).

[21] B. N. Klyarfel'd, L. G. Guseva, and A. S. Pokrovskaya-Soboleva, Zh. Tekh. Fiz. **36**, 704 (1966) [Sov. Phys. Tech. Phys. **11**, 520 (1966)].

[22] I. Pérès, L. C. Pitchford, J. P. Boeuf, H. Gielen, and P. Postma, in *Proceedings of the Sixth International Symposium on the Science and Technology of Light Sources, Budapest, 1992,* edited by L. Bartha and F. J. Kedves (Technical University of Budapest, Budapest, 1992).

[23] Z. Lj. Petrovic and A. V. Phelps, Phys. Rev. E **47**, 2806 (1993); B. M. Jelenkovic, K. Rozsa, and A. V. Phelps, *ibid.* **47**, 2816 (1993); A. V. Phelps, Z. Lj. Petrovic, and B. M. Jelenkovic, *ibid.* **47**, 2825 (1993).

[24] V. I. Kolobov and A. Fiala (unpublished); S. Halló and B. Ngíri, Acta. Phys. Hung. **72**, 71 (1992).

[25] I. Pérès, L. C. Pitchford, and J. P. Boeuf, in *Proceedings of the 11th European Sectional Conference on Atomic and Molecular Physics in Ionized Gases (ESCAMPIG),* edited by L. Tsendin (European Physical Society, Geneva, 1992).

[26] M. J. Druyvesteyn and F. M. Penning, Rev. Mod. Phys. **12**, 87 (1940).

[27] A. R. Gottsho, A. Mitchell, G. R. Scheller, Yin-Yee Chan, and D. B. Graves, Phys. Rev. A **40**, 6407 (1989).

[28] J. P. Boeuf and P. Ségur, in *Interactions Plasmas Froids Matériaux,* edited by C. Lejeune (Les Editions de Phy-

sique, Paris, 1988).
[29] J. P. Boeuf, in *Physics and Applications of Pseudosparks*, edited by M. A. Gundersen and G. Schaefer (Plenum, New York, 1990).
[30] Manoj Dalvie, Satoshi Hamaguchi, and Rida T. Farouki, Phys. Rev. A **46**, 1066 (1992).
[31] G. J. Parker, W. N. G. Hitchon, and J. E. Lawler, Phys. Lett. A **174**, 308 (1993).
[32] M. Dietrich, F. Herrmann, S. Pfau, J. Rohmann, and H. Sievers, in *Proceedings of the XXI International Conference on Phenomena in Ionized Gases (ICPIG)*, edited by G. Ecker (Bochum, Germany, 1993).
[33] R. Schade, Z. Phys. **108**, 353 (1938); H. Buttner, *ibid.* **111**, 750 (1939); A. V. Phelps (private communication).

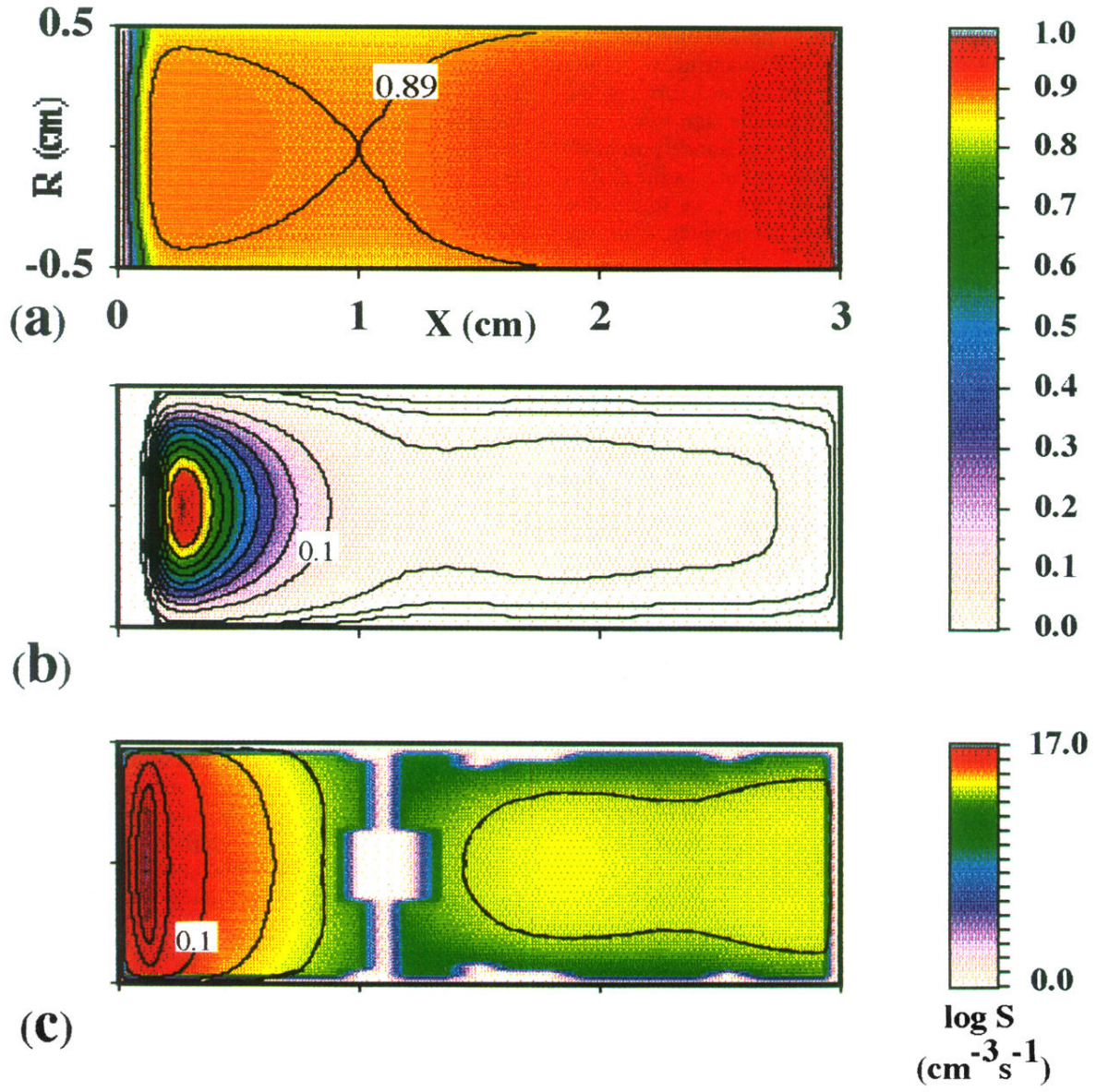

FIG. 9. (a) Contours of constant potential for the positive column point *pc*1 of Fig. 1 in units of 309.7 V; (b) contours of constant electron density for the positive column point *pc*1 in units of 2.9×10^{11} cm^{-3}; (c) contours of constant ionization source term for the positive column point *pc*1 in units of 8.5×10^{16} cm^{-3} sec^{-1}. The contours indicated by the solid lines are equally spaced for the potential and, for the density and source term, the contours are linear between 1.0 and 0.1 and thereafter decrease by factors of 10 per contour.